Progressive Damage Analysis of Post-Buckled Stiffened Panels under Static Compressive Loading

Frank A. Leone[1], Kyongchan Song[2], Cheryl A. Rose[3], Wade C. Jackson[4]
NASA Langley Research Center, Hampton, VA, 23601, United States

The validation of progressive damage analysis methods requires experimental data that captures the initiation of damage, its evolution with continued loading, and the morphology of damage throughout its evolution. In support of the NASA Advanced Composites Project, several validation specimens of increasing complexity have been tested and characterized in order to provide the data required to assess the capabilities of several progressive damage analysis methods for fiber-reinforced composite materials. The analytical capabilities of interest for this validation program include networks of interacting matrix cracks and delaminations in post-buckled stiffened structures. A series of single stringer compression specimens was tested and characterized at NASA Langley Research Center. The experimental data from these tests are compared with progressive damage finite element analysis results. Test/analysis comparisons are made in terms of load/displacement histories, damage morphology, and damage size versus load metrics.

I. Introduction

The certification of aircraft structures composed of fiber-reinforced composite materials involves a large amount of structural testing. These tests range in scale from small material characterization coupons to full-scale structural fatigue and residual strength tests, with several levels of increasing size and complexity in between. In order to promote the adoption of composite materials in primary and secondary aircraft structural designs, it is necessary to reduce the amount of testing required for aircraft certification. Progressive damage analysis (PDA) methods claim to be able to predict failure in composite structures, including the initiation and progression of damage up to ultimate failure. These predictive tools have the capability to reduce the amount of testing required to certify aircraft structural components. Many PDA tools for composite materials have been developed by researchers and engineers in the commercial, academic, and government sectors. However, prior to the aircraft industry accepting these predictive methods into their structural certification process, it is necessary to increase their confidence in the capabilities of these tools and to gain a better understanding of the strengths and weaknesses of specific PDA methods and assumptions.

As part of the NASA Advanced Composites Project (ACP), a verification and validation (V&V) framework for PDA methods for composite materials has been developed and applied for several down-selected methods [1]. One of the structural problems of interest to the ACP is a post-buckled stiffened panel subjected to barely visible impact damage, realized as a four-stringer panel subjected to compressive longitudinal loading [2]. As part of the V&V framework, several structural configurations of increasing complexity from simple coupons to the four-stringer panel have been considered and evaluated in a building block format. The first problem configuration in the building block approach is a doubler-stiffened coupon subjected to three-point bending loading, presented in Ref. [3], which exhibits interacting matrix crack and delamination damage modes. The second element in the validation building block is a hat-stiffened seven-point bending specimen, presented in Ref. [4], which is loaded into a post-buckled-like shape and

---

[1] Research Aerospace Engineer, Durability, Damage Tolerance, and Reliability Branch.
[2] Research Aerospace Engineer, Structural Mechanics and Concepts Branch, Member.
[3] Senior Research Aerospace Engineer, Durability, Damage Tolerance, and Reliability Branch, Member.
[4] Senior Research Aerospace Engineer, Durability, Damage Tolerance, and Reliability Branch, Member.

exhibits stable damage growth throughout its loading history. The penultimate structural configuration in the validation building block is a post-buckled panel with a single hat stiffener subjected to longitudinal compressive loading, i.e., the single stringer compression specimen, presented herein. Some of the challenges first encountered while considering the single stringer compression specimen in the validation building block approach include:

- predicting the onset of buckling and the correct post-buckled mode shape;
- experimentally characterizing and predicting the rapid development of damage before unstable propagation under high compressive loads [5]; and
- the volume of material that could be reasonably expected to develop damage, and the associated computational cost of PDA methods due to their often small (e.g., < 0.01 inch) mesh size requirements [6].

This paper is organized as follows. First, the details of the single stringer compression specimen are presented, along with the details of the experimental testing procedure. Next, one of the PDA methods evaluated as part of the ACP V&V framework is introduced, and the finite element (FE) analysis details are presented. Finally, a selection of test and analysis results are presented and discussed.

II. Experimental Specimens and Testing

The single stringer test specimens are composed of a fiber-reinforced polymer tape laminate skin panel and a single, co-cured hat stiffener. The specimens are 20.2 inches in length (i.e., along the stiffener) and 8.5 inches wide. The skin panel is a 12-ply laminate composed of IM7/8552 unidirectional tape material with a $[+45/-45/0/90/+45/-45]_S$ stacking sequence. The hat stiffener is composed of IM7/8552 plain-weave (PW) fabric and consists of a 4-ply interior wrap and a 12-ply overwrap, which forms the stiffener flanges. The stacking sequence of the stiffener interior wrap is [+45/−45/0/+45], interior to exterior. The stacking sequence of the stiffener overwrap is [+45/−45/0/+45/+45/0/−45/+45/+45/−45/0/+45], interior to exterior. The 0° direction is parallel to the stiffener length. The hat stiffener, flange edge to flange edge, is 4.3 inches wide. The intersections of the skin panel, stiffener interior wrap, and stiffener overwrap, i.e., the noodle regions, are filled with additional adhesive material. The top and bottom loading surfaces of the specimens have 1.5 inches of potting material, machined flat and parallel. In addition, additional tabbing material reinforces the skin panel and stiffener flanges for 3.6 inches along the stiffener away from either load application surface. The additional tabbing material avoids failures in the load application region and causes the skin panel to buckle in the central 13-inch-long gage section.

The single stringer compression specimens were tested in a 100-kip load frame under displacement control. A single stringer specimen in a load frame is shown in Fig. 1. Each specimen had six pairs of back-to-back uniaxial strain gages oriented in the loading direction to monitor the symmetry of loading. Two three-dimensional digital image correlation (DIC) systems were used to monitor the buckling mode shape, one on the stiffener side and one on the skin side. Acoustic emission (AE) sensors and a passive thermography system were used to monitor for damage progression events [5].

Each specimen was initially loaded until the skin panel buckled to determine the sign and shape of its particular post-buckling mode. After identifying the post-buckled shape of each specimen, an interrupted testing approach was adopted in order to generate sufficient experimental data to validate the predictions of the analyses. Specimens were loaded until one of the data acquisition methods gave an indication of possible damage growth, at which point the specimens were rapidly unloaded and removed from the load frame. After unloading, ultrasound (UT) and X-ray computed tomography (CT) scans characterized the new specimen damage state. After completing the scans, the specimen was returned to the load frame, and the test was continued. The test plan was to repeat this loading-unloading-characterizing cycle until a significant amount of damage was observed; however, each specimen was loaded to ultimate failure due to the rapid progression of damage in the specimens.

Prior to testing, the dimensions and initial shape of each specimen were measured both manually and using a coordinate measurement machine. Manual measurements included skin panel and stiffener flange thickness and width measurements at multiple locations. Pre-test UT scans were performed for all specimens to characterize the extent of any initial damage. The experimental testing matrix includes specimens with three initial conditions:

1. Pristine
2. Teflon
3. Impact

The pristine specimens contain no known internal flaws. The Teflon specimens contain 0.25-inch-wide Teflon inserts between the stiffener flanges and the skin panel. The Teflon inserts run the full length of the stiffener and are located along the outer ends of the stiffener flanges. The Teflon inserts represent an initial damage state, with a damage severity similar to that resulting from a low-velocity impact event.

The impact specimens were impacted on the skin-side along the stiffener flange termination. Prior to impacting, specimens were loaded to low load levels to determine their post-buckled shape. The longitudinal location of the impacts corresponds to a location where the post-buckled shape causes the skin to buckle away from the stiffener flange. Drop weight impacts were conducted with an impactor with a 1-inch-diameter hemispherical stainless steel tip and a mass of 3.82 lbm. Impact energies ranged from 3.75 to 4.00 ft-lbs, as calculated from drop height.

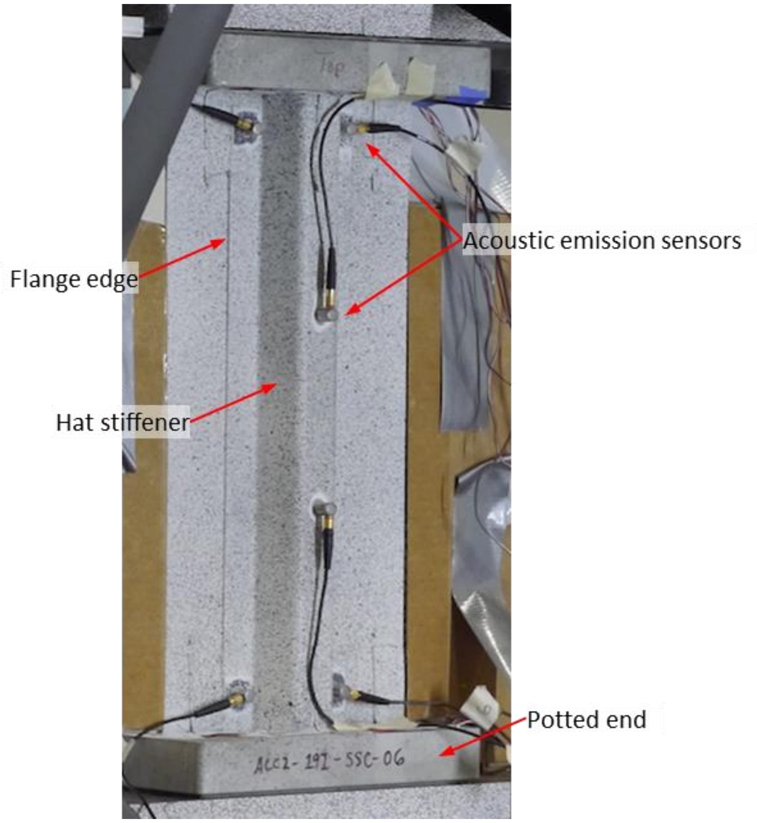

Fig. 1 Single stringer compression specimen.

III. Progressive Damage Finite Element Analyses

Several finite element models with increasing levels of fidelity were developed for the progressive damage analysis of the single stringer compression specimens. First, a FE model of the single stringer compression specimen was developed for use in implicit buckling mode analyses. In this model, linear elastic materials were defined throughout, and the Lanczos eigensolver was used to estimate the first ten eigenvalue buckling modes. Next, a FE model was developed that included interlaminar damage on the skin/stringer interface using cohesive elements. This single-interface model was used for pretest analyses, to simulate the global structural response, and to predict onset of damage. Based on these initial global buckling analyses and damage predictions, the boundary conditions and overall analysis procedure were validated. Finally, a FE model of the single stringer compression specimen with a highly refined mesh in the areas of interest was developed to predict the onset and progression of damage through the skin/stringer interface and the skin laminate. This paper focuses on the more highly refined FE model, its results, and comparisons with the measured experimental damage states.

A. Progressive Damage and Failure Analysis Methods

Multiple PDA methods have been applied as part of the NASA ACP V&V efforts, including methods representative of the continuum damage and discrete damage mechanics method classes. Custom elements and constitutive material models are included in the effort, as well as methods designed for implicit and explicit FE formulations. PDA methods with all combinations of these different assumptions and formulations have been able to represent the onset and evolution of damage in the validation problems considered in the validation building block. In this paper, only select results made with the CompDam continuum damage mechanics constitutive material model [7] are presented.

CompDam is a VUMAT user material subroutine compatible with the commercial FE solver Abaqus/Explicit. The continuum damage mechanics based material model specializes in representing the kinematics of embedded matrix cracks in a highly deformed continuum. The CompDam material model has capabilities related to fiber tensile failure, fiber kink band modeling, pre-peak nonlinearities, and others, but only the matrix crack and delaminations capabilities are the focus of this work. The CompDam source code is released open source under the NASA Open Source Agreement v1.3. The source code is hosted on the NASA GitHub site at https://github.com/nasa/CompDam_DGD/. CompDam v2.5.0 was used for all of the analysis results presented in this paper.

B. Finite Element Model

A part-based assembly approach is used to construct the FE model of the single stringer compression specimen. The model comprises continuum shell, solid, and cohesive elements, as shown in Fig. 2. Damage predictions are made in a central 12.5-inch-long by 5-inch-wide refined section of the skin panel and skin/stiffener interface. The hat stiffener overwrap, the hat stiffener inner wrap, the reinforcement tabs, and the portion of the skin panel outside the central damage region are orthogonally meshed with SC8R continuum shell elements. The refined region of the skin panel in which damage predictions are made contains only the top two plies and interfaces of the skin panel. The lower ten plies of the skin laminate in the refined region are modeled with a single layer of continuum shell elements. The skin/stiffener interface is meshed with a single layer of cohesive elements. The noodle regions are filled with six-node and eight-node solid elements. Tie constraints are used throughout the assembly to connect the adjacent parts.

PDA methods generally require a finer discretization than is required to achieve converged FE solutions in terms of just deformed shape, stiffness, or stress. CompDam is intended to be applied to layers of solid elements that represent the response of individual plies, so a ply-by-ply meshing strategy is applied in the refined central section of the skin panel. One-element-thick layers of C3D8R solid elements are used to represent the skin panel plies for damage predictions. Enhanced hourglass and distortion control are used for the reduced-integration solid elements. The mesh lines of solid-element parts are aligned with the local fiber directions so that matrix cracks do not grow across fibers and to avoid any sensitivity of the predictions to mesh misalignment [8]. Furthermore, to better represent the local stress field ahead of matrix cracks, matrix cracking is limited to every third row of elements within each ply part [9]. Cohesive elements are inserted between the solid-element ply parts to represent internal skin panel delaminations. The nodes of adjacent solid-element ply and cohesive-element interface layers are not coincident, so tie constraints are used to connect the alternating solid and cohesive element layers. An exploded view of the fiber-aligned solid-element layers and cohesive layers is shown in Fig. 3. A uniform in-plane element edge length of 0.00787 inch is used in the solid element ply parts, the interlaminar cohesive skin panel parts, and the skin/stiffener interface cohesive layer.

The material properties used for the IM7/8552 PW fabric material used in the stiffener are shown in Table 1. Damage predictions were not performed for the fabric material, so only orthotropic stiffness properties were required. Composite shell section definitions are used to define the response of the elements in the fabric stiffener.

Table 1. IM7/8552 PW Fabric Material Properties

E_1, psi	E_2, psi	ν_{12}	G_{12}, psi	G_{13}, psi	G_{23}, psi
9.58e+6	9.55e+6	0.052	0.738e+6	0.492e+6	0.492e+6

The stiffness, strength, and fracture toughness material properties used for the IM7/8552 unidirectional tape material used in the skin panel are found in Table 2. The strength and fracture toughness properties for the unidirectional tape are used for predictions of both intralaminar matrix cracks and internal delaminations within the skin panel.

Table 2. IM7/8552 Tape Material Properties

E_1, psi	E_2, psi	ν_{12}	ν_{23}	G_{12}, psi	Y_T, psi
21.3e+6	1.26e+6	0.32	0.45	0.749e+6	11.6e+3
S_L, psi	**G_Ic, lbf/in**	**G_IIc, lbf/in**	**η**	**Y_C, psi**	**α_0, °**
14.2e+3	1.37 [10]	4.22 [11]	2.1 [12]	41.8e+3	53 [13]

The interface between the unidirectional tape skin panel and the PW fabric stiffener has different fracture properties than the internal tape/tape interfaces of the skin panel. While no appreciable crack growth resistance curve was observed for the tape/tape interface, the fracture response of the tape/fabric interface becomes tougher as the damage grows. Two sets of tape/fabric interface properties are used in the analyses presented herein, corresponding to the measured damage onset (G_{c}) and the steady-state damage progression (G_{R}) values, Table 3.

Table 3. Tape/Fabric Interface Fracture Toughness Properties

Damage onset (G_{c})			**Damage progression (G_{R})**		
G_{Ic}, lbf/in	**G_{IIc}, lbf/in**	**η_{c}**	**G_{IR}, lbf/in**	**G_{IIR}, lbf/in**	**η_{R}**
1.68	7.01	1.3	3.32	8.01	0.5

The Teflon and impact damage analyses require the definition of initial damage states. The 0.25-inch-wide Teflon inserts are represented with the CompDam material model by setting the matrix damage state variable equal to one, i.e., fully damaged, in the skin/stiffener interface cohesive elements as an initial condition. All other damage model state variables are initialized to their nominal values for this case. The impact damage configuration requires the initialization of damage on the skin/stiffener interface, the internal skin panel interfaces, and within skin panel plies. The experimental impact damage was characterized by UT and X-ray CT. The damage scan data were incorporated by manually defining sets of solid elements for the matrix cracks and sets of cohesive elements for the delaminations. UT data were used to define the delamination element sets and X-ray CT data were used to define the matrix crack element sets. Aside from the initialization of damage state variables, the pristine, Teflon, and impact damage model inputs were identical.

A single explicit dynamic step of 0.2 second duration is used to load the specimen. Variable mass scaling is applied at every solution increment to maintain a time increment of 2.5×10^{-7} second. The time and mass scaling parameters of the analysis step were selected to maintain quasi-static conditions while remaining computationally tractable. Velocity-based boundary conditions are applied to the nodes on the top and bottom surfaces (as oriented in Fig. 2a) to apply 0.1 inch of compressive displacement along the stiffener length during the step. The amplitude of the applied velocities increases to a constant value over 10% of the step duration according to a smooth step function. The top and bottom surfaces are displaced in opposite directions to minimize the kinetic energy introduced into the system, with each surface moving one-half of the prescribed displacement. In order to control the post-buckled shape of the models in the explicit analyses, initial geometric imperfections are defined with a shape based on the earlier implicit buckling mode analysis results.

The full FE mesh contains approximately 5.1×10^{6} elements and has 3.1×10^{7} degrees of freedom. Domain decomposition was used to decompose the model into 400 domains, and the analyses were solved on the NASA Langley K4 cluster, described further in Ref. [14]. With the selected combination of time scaling, mass scaling, and the degree of parallelization on the K4 cluster, analysis run times ranged from 10 to 16 hours when run with 400 cores. The explicit analyses progressed at relatively steady rates in terms of step time per wall clock time, and the run times are roughly proportional to the applied displacement at the end of each analysis. All of the analyses ended after the onset of unstable damage propagation due to either numerical issues or excessive element distortion errors, when the assumptions of quasi-static loading had already been invalidated by the rapid damage growth and structural unloading.

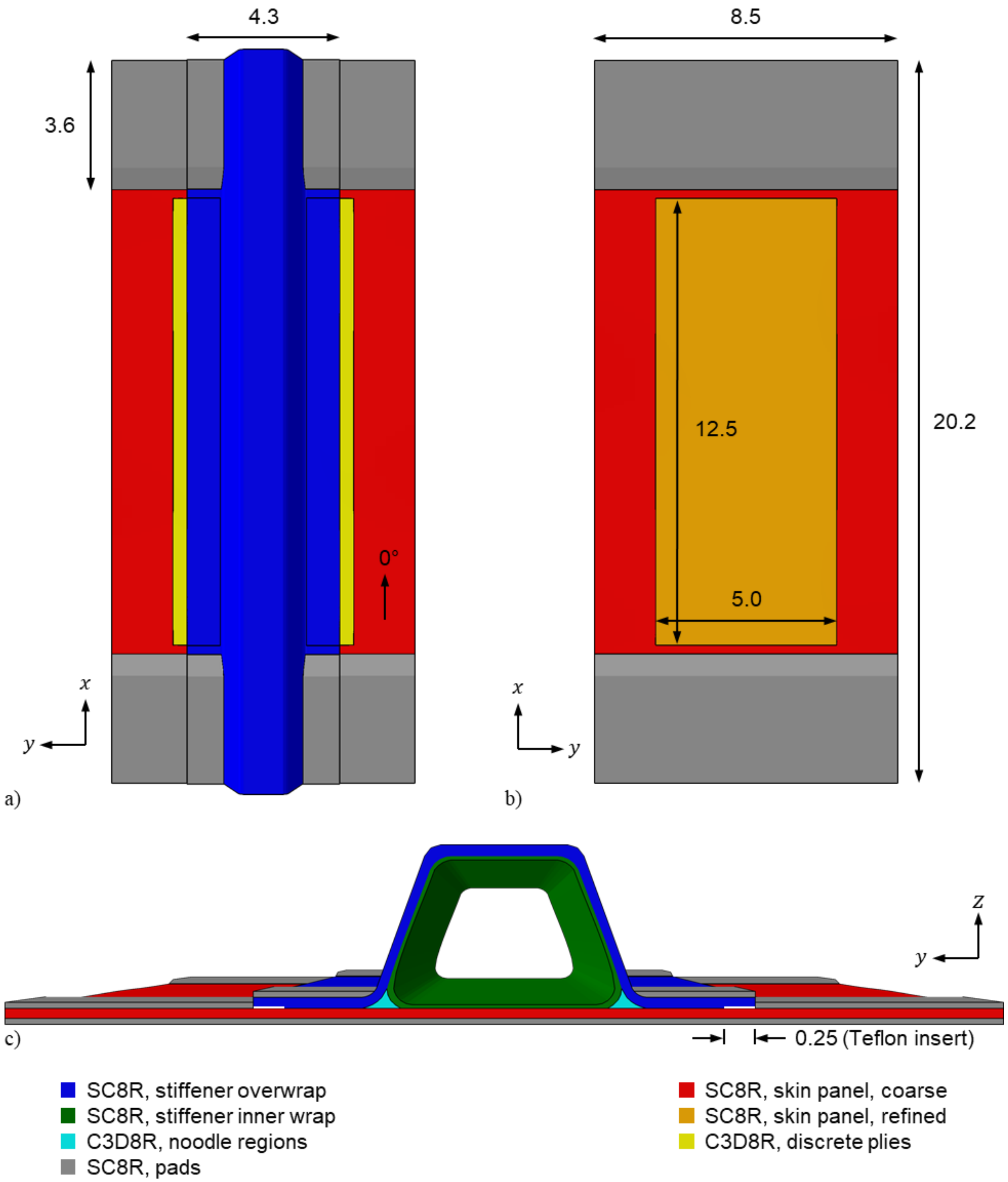

Fig. 2 Single stringer compression specimen FE model. All dimensions in inches.

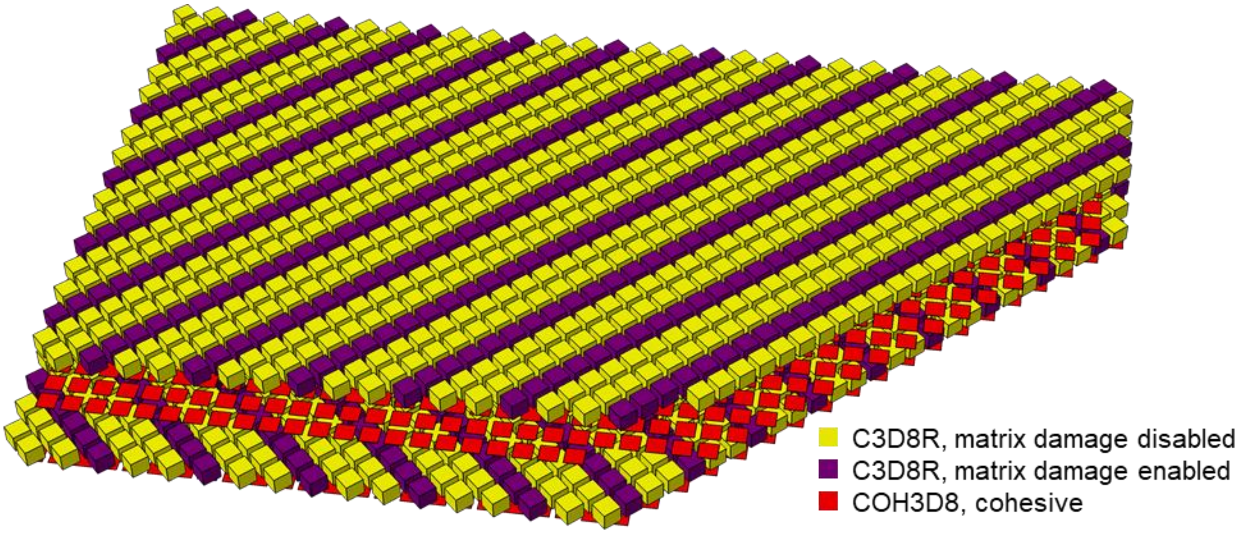

Fig. 3 Ply-by-ply discrete meshing strategy for refined region of the skin panel in the FE model. The top two plies and interfaces of the skin panel are shown. The elements are shrunk for clarity.

IV. Results

During testing, multiple buckling modes were observed for nominally identical specimens of the same initial condition. For the specimens tested, the two buckling mode shapes that were observed most frequently contained:

I. Three half-waves in each half of the skin panel, with the center half-waves buckling away from the stiffener, and the outer two half-waves buckling toward the stiffener
II. Three half-waves in each half of the skin panel, with the center half-waves buckling toward the stiffener and the two outer half-waves buckling away from the stiffener

These two buckling modes are referred to herein as the “Type I” and “Type II” buckling shapes, respectively, and are shown in Fig. 4. Type I and Type II buckling shapes were observed for the testing of the pristine and Teflon specimens. A single impact case is presented herein, which exhibited Type II buckling shape.

A summary of the experimental specimens for which results are presented in this paper is in Table 4. The following sub-sections will present and discuss select experimental and analysis results for these pristine, Teflon, and impacted configurations of the single stringer specimens. For each experimental configuration in Table 4, PDA results for models using the G_c and G_R tape/fabric interface properties are presented.

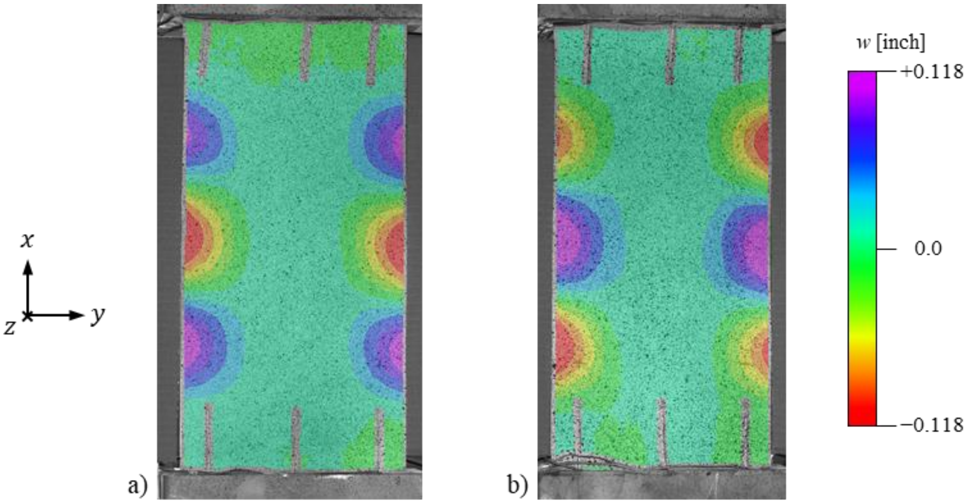

Fig. 4 Single stiffener buckling shapes on the skin surface: (a) Type I and (b) Type II.

Table 4. Experimental Results Summary

Specimen No.	**Buckling Mode**	**Initial Condition**	**Peak Load, kip**
SSC-06	Type I	Pristine	−44.7
SSC-05	Type II	Pristine	−50.7
SSC-02	Type I	Teflon insert	−34.1
SSC-01	Type II	Teflon insert	−30.5
SSC-04	Type II	Teflon insert	−30.6
SSC-03	Type II	Impact	−38.4

A. Pristine

The experimental and analytical load/displacement histories for the pristine single stringer compression specimens exhibiting the Type I buckling shape are shown in Fig. 5. Specimen SSC-06 exhibited the Type I buckling mode and was loaded monotonically to failure at a peak load of −44.7 kip. The G_c and G_R analyses predict peak loads of −39.6 and −45.0 kip, respectively, bounding the experimental result.

Because specimen SSC-06 was loaded monotonically to failure, there is no intermediate nondestructive damage evaluation data for this specimen. The analysis results, however, do predict the initiation and stable growth of damage prior to ultimate failure. The analytical load/displacement histories in Fig. 5 are annotated with the first instances of elements becoming fully damaged in different parts of the laminate (e.g., the skin/stiffener interface, the first skin ply). For both analyses, damage is predicted to initiate as matrix cracking in the top ply of the skin, underneath the stiffener flange termination. Maps of the predicted damage states are provided in Fig. 6. The damage map figures show only fully damaged elements, and the colors in the plots correspond to the interface the damage is on (i.e., blue is damage on the skin/stiffener interface, red is damage on the first interface of the skin panel, and purple is damage on both interfaces). The damage initiated at the location where the post-buckled shape causes the skin to buckle away from the stiffener, introducing mode I loading to the skin/stiffener interface. The G_c analysis predicted delamination growth in the skin/stiffener interface (Fig. 6a) and migrations down to the first interface of the skin panel via 45° matrix cracks (Fig. 6b). The tougher skin/stiffener interface in the G_R analysis limited the pre-peak damage growth to matrix cracking and skin panel delaminations (Fig. 6c), with the initiation of damage in the skin/stiffener interface (Fig. 6d) leading to the predicted load drop. The analytical damage morphology is very similar to that predicted for the pristine seven-point bend specimens tested and analyzed as part of the NASA ACP, reported in detail in Ref. [4].

Specimen SSC-05 exhibited the Type II buckling shape and was loaded five times before ultimately failing, Fig. 7. Run four out of five had the highest peak load of −50.7 kip, and the specimen failed during the fifth loading at −44.9 kip. The specimen was inspected using ultrasound and X-ray CT after the first four loadings, but no damage was detected at the skin/stiffener interface. Damage was detected by X-ray CT in the stiffener, but this damage was not accounted for in the analyses. The G_c and G_R analyses predicted peak loads of −33.0 and −35.5 kip, respectively, significantly lower than the maximum applied experimental load. Both analyses predict damage to initiate in the form of matrix cracking in the first and third post-buckled half-waves, in which peel loading of the skin/stiffener interface occurs. After initiation, the predicted damage morphologies in the opened half-waves are similar to the damage morphologies in the corresponding Type I buckling shape analyses. The predicted damage maps of the two analyses are shown in Fig. 8, showing the damage immediately before and after the onset of unstable damage propagation.

To quantify the initiation and growth of damage within the tests and analyses, measurements of the damage length along the stiffener flange terminations were made. The test and analysis damage lengths for the Type I and Type II buckling shapes are shown in Fig. 9a and Fig. 9b, respectively. The experimental measurements (black lines with yellow markers) were manually performed based on the UT scan data. The analytical damage lengths are the maximum distance between two fully damaged elements within each post-buckled half-wave (two lengths per specimen for Type I and four lengths per measurements for Type II, Fig. 4). The experimental curves show zero damage length until structural failure. The analysis curves show that the G_c analyses predicted faster damage growth rates and larger pre-peak damage lengths than the corresponding G_R analyses. Another damage growth difference between the G_c and G_R analyses that is not shown in Fig. 9 involves the maximum depths of the damage (i.e., the distance the damage extended underneath the stiffener, toward the stiffener centerline) prior to failure. The pre-peak G_c analysis damage maps (Fig. 6a and Fig. 8a) show a multi-interface damage state growing both along and underneath the stiffener flange. The G_R analysis damage maps (Fig. 6c and Fig. 8c) instead show almost no increase in the damage depth prior to failure.

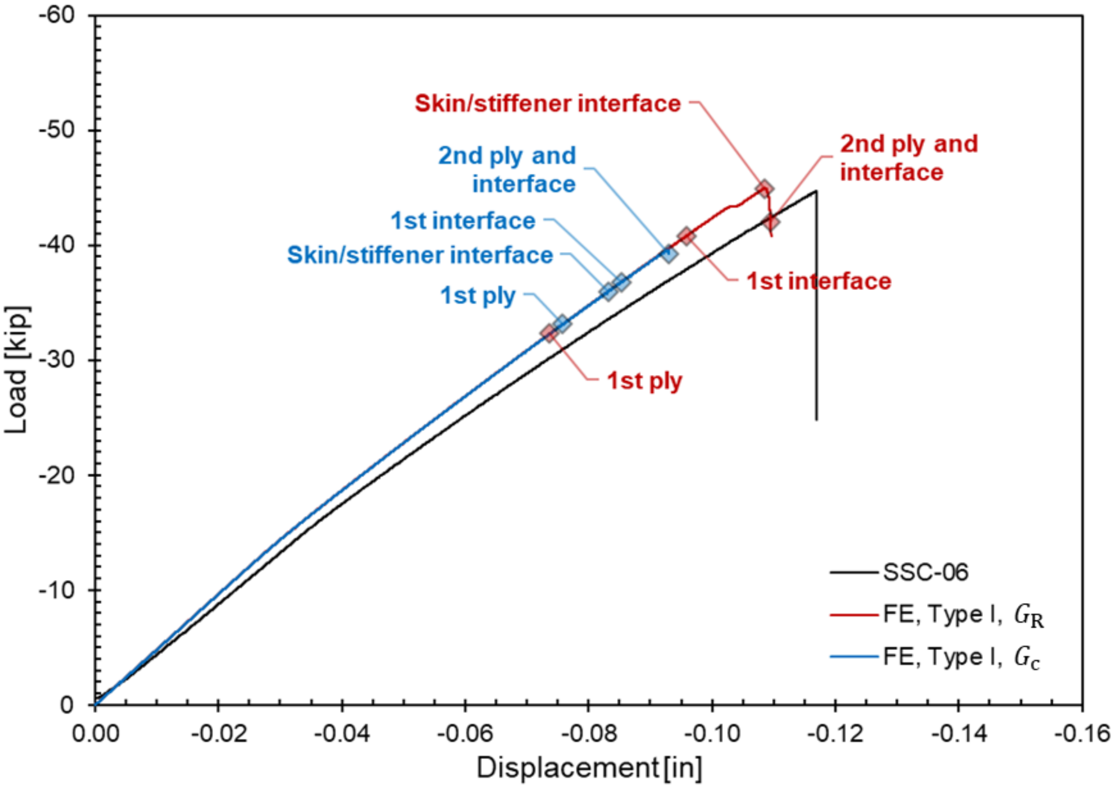

Fig. 5 Test and analysis load/displacement histories for pristine specimens with the Type I buckling shape.

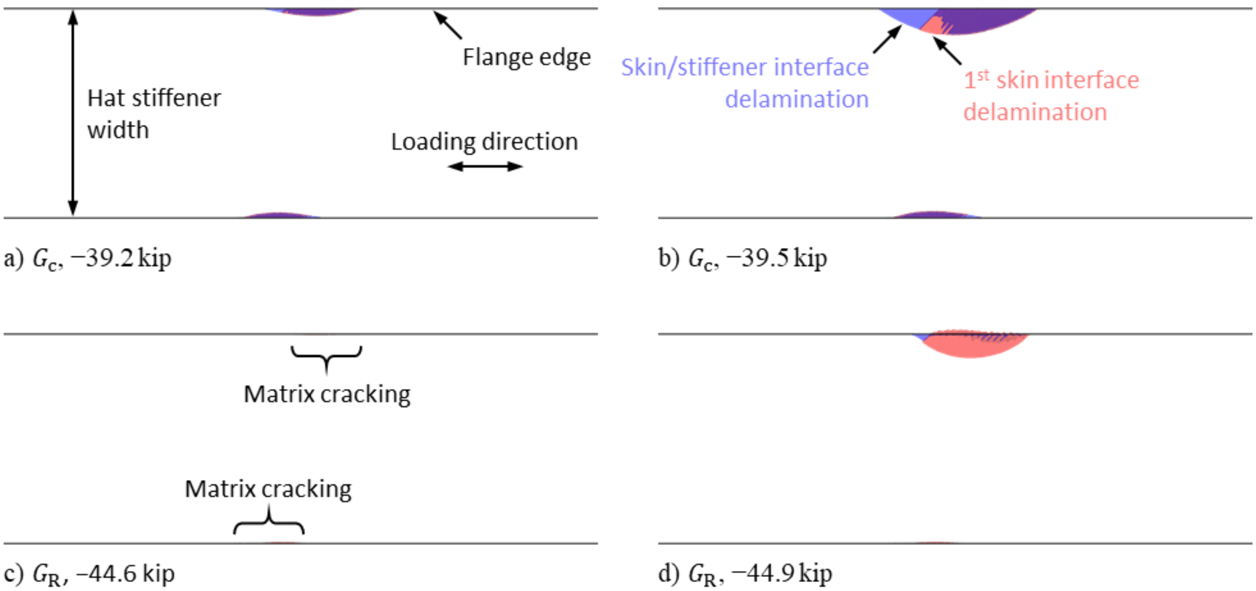

a) G_c, −39.2 kip

b) G_c, −39.5 kip

c) G_R, −44.6 kip

d) G_R, −44.9 kip

Fig. 6 Damage maps for pristine specimen analyses with Type I buckling shape and two tape/fabric interface property sets (G_c and G_R).

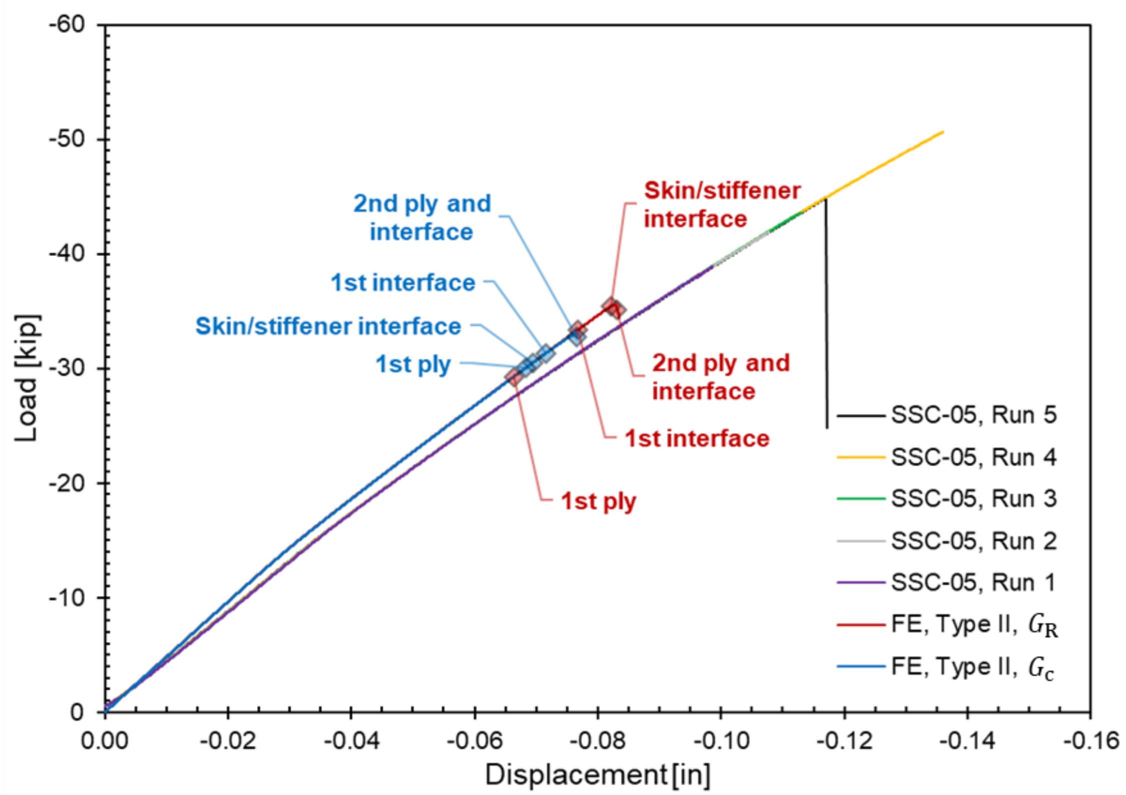

Fig. 7 Test and analysis load/displacement histories for pristine specimens with the Type II buckling shape.

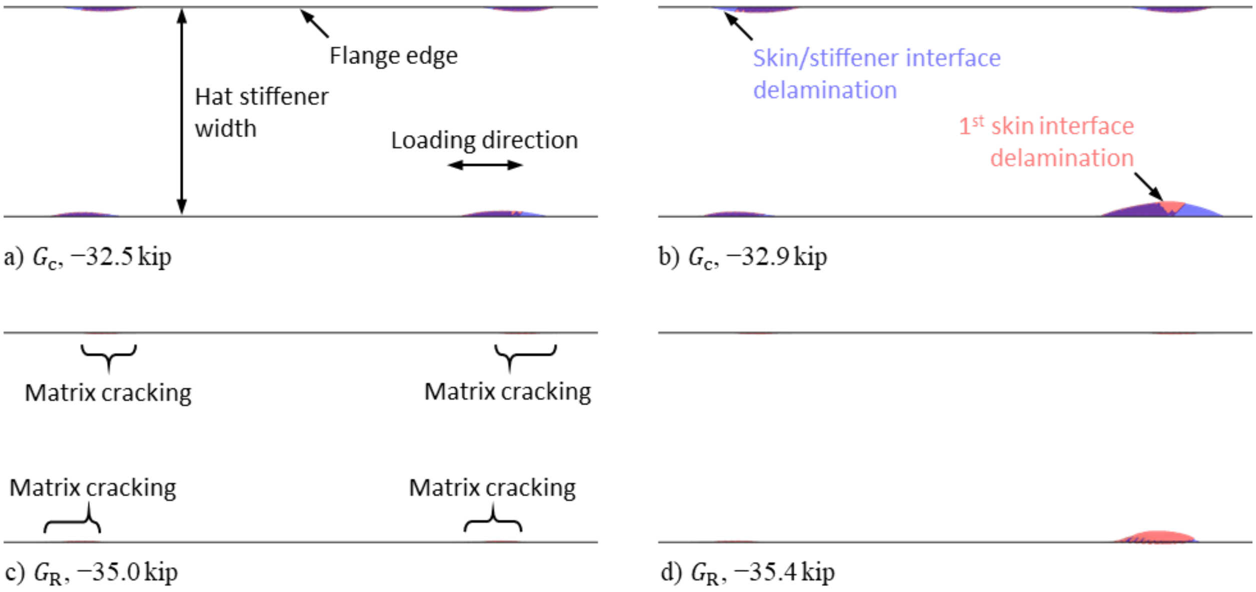

a) G_c, −32.5 kip

b) G_c, −32.9 kip

c) G_R, −35.0 kip

d) G_R, −35.4 kip

Fig. 8 Damage maps for pristine specimen analyses with Type II buckling shape and two tape/fabric interface fracture property sets (G_c and G_R).

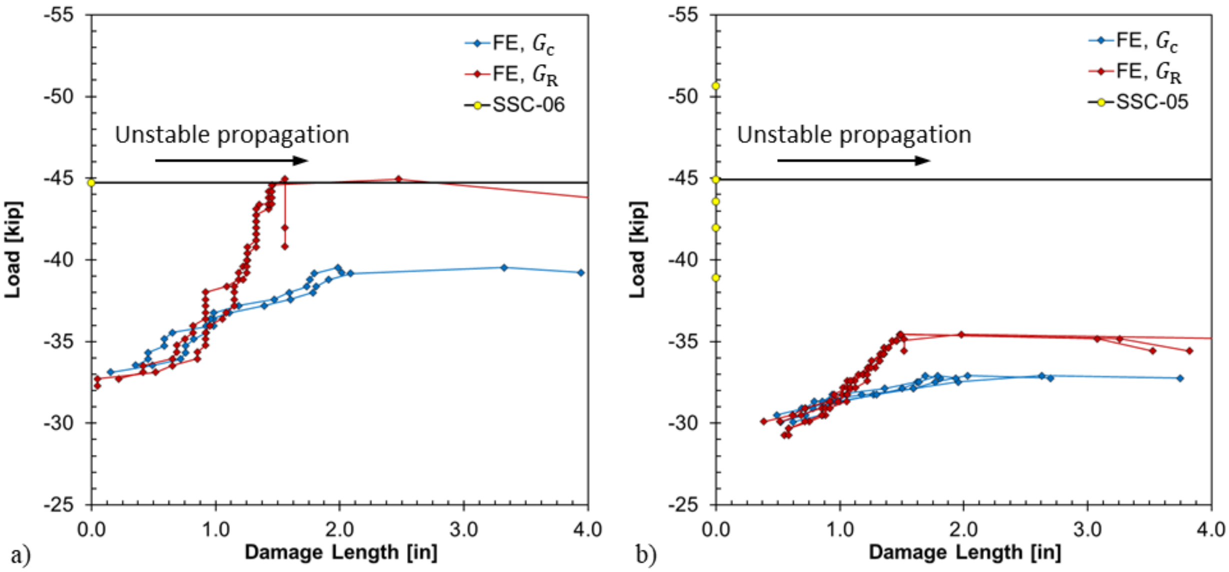

Fig. 9 Load versus damage length for pristine tests and analyses for the (a) Type I and (b) Type II buckling shapes. Damage lengths are measured along the length of the stiffener flange edges.

B. Teflon insert

Specimen SSC-02 exhibited the Type I buckling shape. The specimen was loaded three times, ultimately failing during the third loading at a peak load of −34.1 kip. The load/displacement histories of the three loadings of specimen SSC-02 are shown in Fig. 10. The experimental displacements used to populate Fig. 10 are taken directly from the load frame, and the experimental load/displacement curves are shifted so that their initial linear slope passes through the origin. Predicted load/displacement curves from analyses using the G_c and G_R tape/fabric interface properties are also plotted. The peak loads of the G_c and G_R analyses are −33.4 and −35.1 kip, respectively, closely bounding the experimental peak load.

Unlike in the pristine tests, nondestructive inspection of the Teflon-insert specimens during the interrupted loadings provided data on the initiation, morphology, and growth of the damage. The UT scan amplitude plots of specimen SSC-02 are provided in Fig. 11, and the predicted damage maps from the Type I buckling shape analyses are provided in Fig. 12 for the G_c properties and Fig. 13 for the G_R properties. The UT and analysis results are plotted at the same length scale. The analytical damage maps are taken from the output frames at which the model reaction load most closely matches the experimental peak load of the corresponding test. Within the UT data, the 0.25-inch-wide Teflon strips are visible along the top and bottom of the scans, and the dark horizontal bands are the noodle regions of the hat stiffener. After Run 1, the experimental damage comprises semi-elliptical delaminations split along the skin/stiffener interface and the first interface of the skin panel, connected by a series of 45° matrix cracks, Fig. 11a. A qualitative visual comparison of the damage after Runs 1 and 2 (Fig. 11b) shows no significant change in the damage length along the stiffener and a slight increase in the depth of the damage underneath the stiffener. The G_c damage maps match the test results in terms of damage morphology and size. The predicted evolution of damage in the analysis is more gradual than the experimentally observed three steps to failure. The composition of the pre-peak damage in the G_R analysis in Fig. 13 differs from the tests and the G_c analysis results, containing predominantly matrix cracks along the stiffener flange terminations until damage propagates unstably on the first interface of the skin panel.

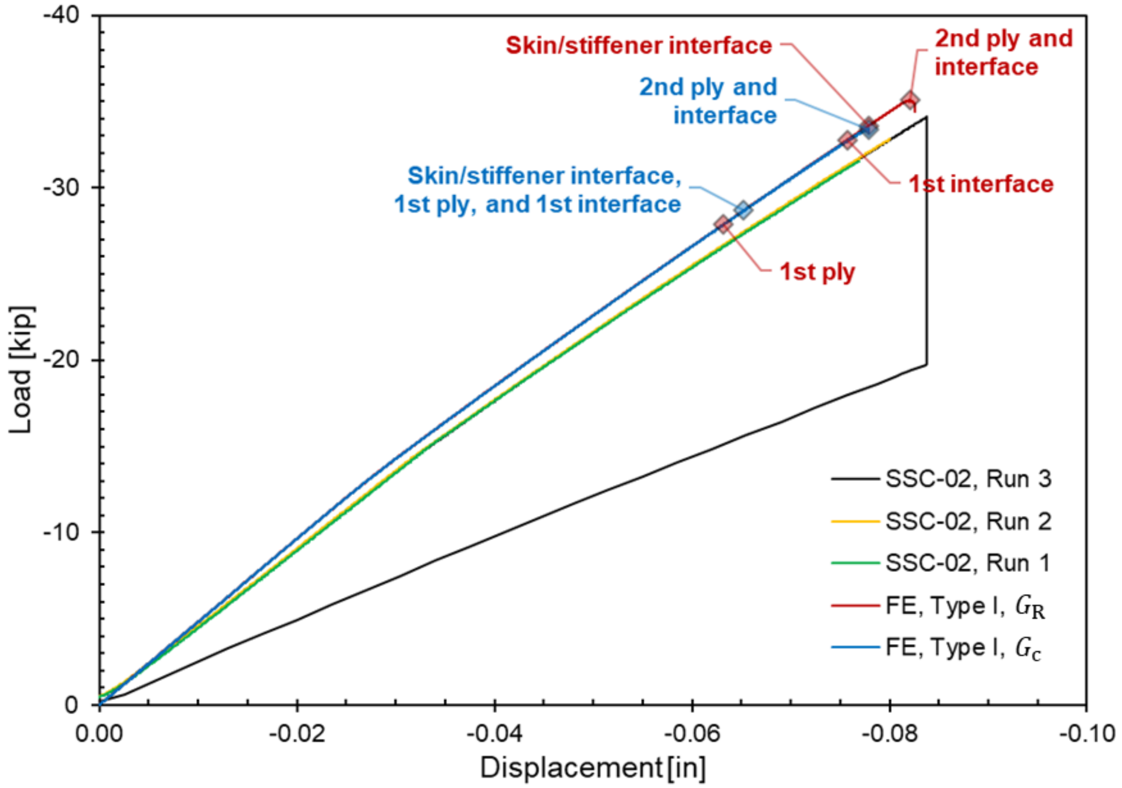

Fig. 10 Test and analysis load/displacement histories for Teflon specimens with the Type I buckling shape.

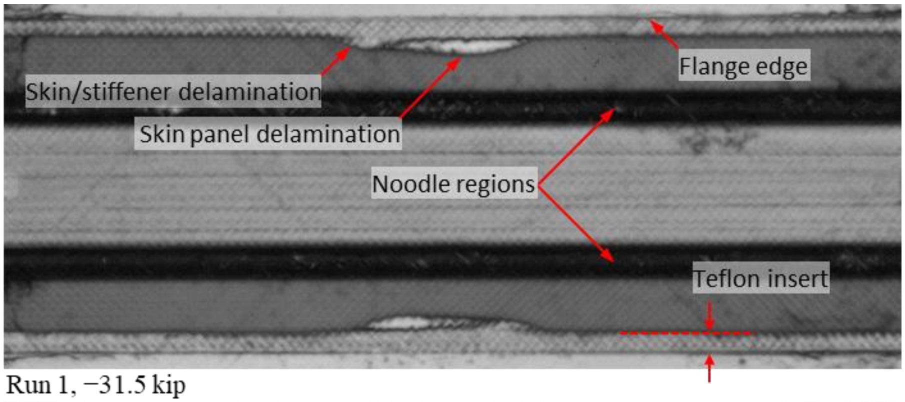

a) Run 1, −31.5 kip

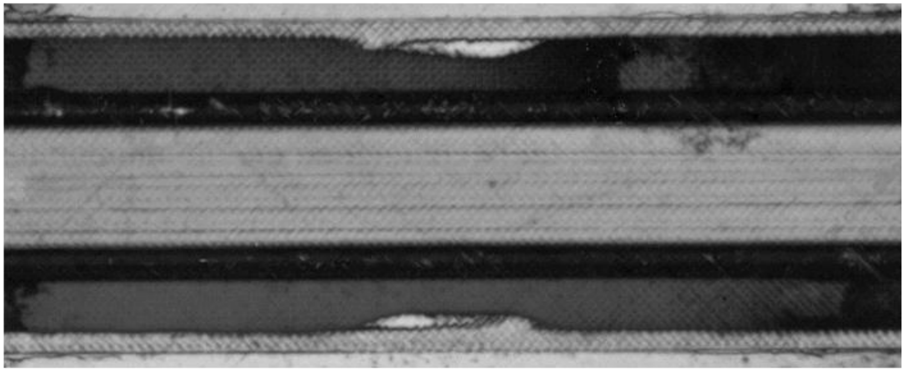

b) Run 2, −32.8 kip

Fig. 11 UT scans for Teflon specimen SSC-02, with the Type I buckling shape.

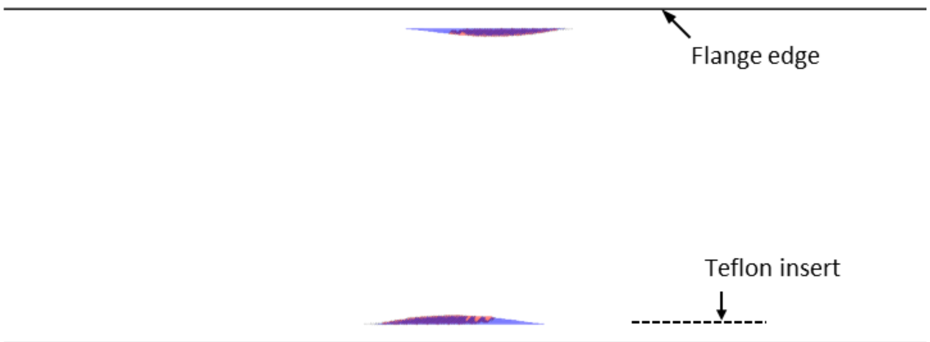

a) −31.6 kip

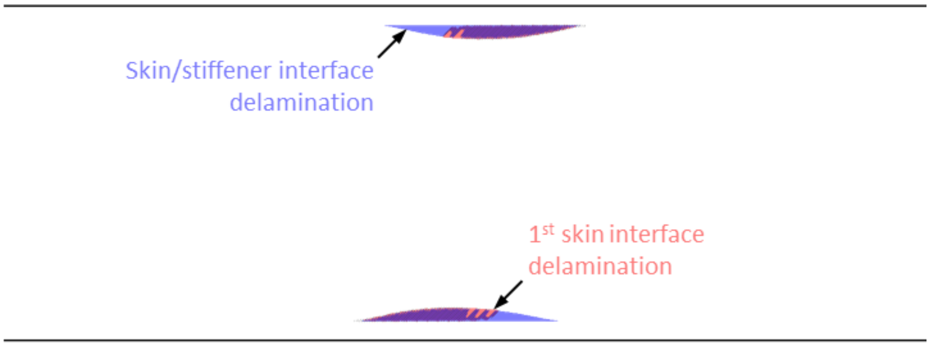

b) −32.7 kip

Fig. 12 Damage maps for Teflon analyses with Type I buckling and G_c tape/fabric interface properties.

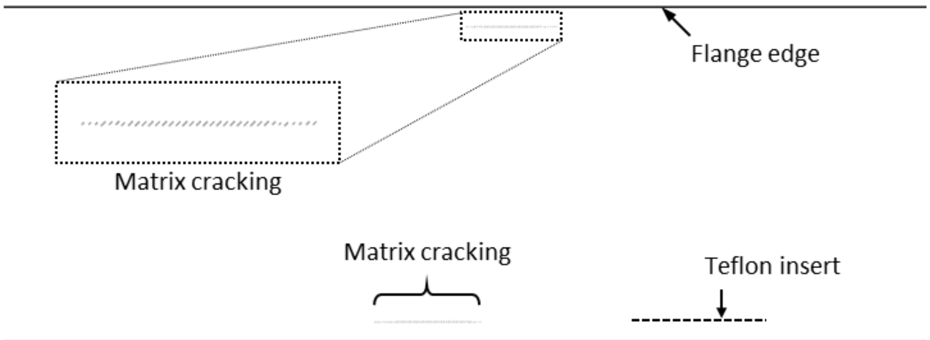

a) −31.6 kip

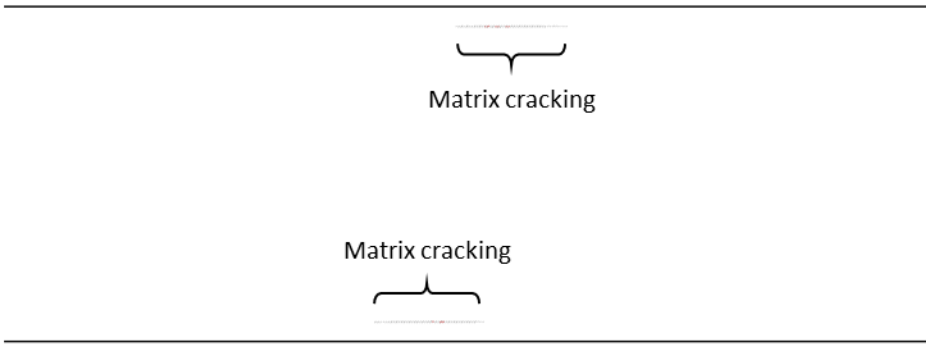

b) −32.8 kip

Fig. 13 Damage maps for Teflon analyses with Type I buckling and G_R tape/fabric interface properties.

Teflon specimens SSC-01 and SSC-04 exhibited the Type II buckling shape. Specimen SSC-01 was loaded directly to failure, reaching a maximum load of −30.5 kip, while the loading of specimen SSC-04 was interrupted to scan for changes in the damage state, ultimately failing at a peak load of −30.6 kip on the fifth loading. The load/displacement histories of these two specimens are shown in Fig. 14. Both specimens buckled around −15.0 kip applied compressive load, causing a slight change in the stiffness response. The UT scans of specimen SSC-04 after the first three loadings are provided in Fig. 15; no significant growth was observed between the third and fourth loading. The damage initiated and grew anti-symmetrically, in one of the three half-waves on each side of the stiffener. The damage morphology initially comprised only delamination in the skin/stiffener interface, then migrated to the first interface of the skin panel via a series of matrix cracks. The damage grew both along the stiffener length and inwards, underneath the stiffener flanges. The maximum observed depth of the damage is approximately one-half of the stiffener flange width, as seen in the bottom-right corner of Fig. 15c.

The peak loads of the Type II buckling shape Teflon specimen analyses with the G_{c} and G_{R} tape/fabric interface fracture properties are −29.4 and −31.1 kip, respectively. The analytical load/displacement responses do not possess any features that correspond to the initiation of damage. Prior to the predicted load-drops, however, plateaus develop in the load/displacement response of both analyses. The predicted damage maps from the Type II buckling shape analyses with the G_{c} and G_{R} tape/fabric interface properties are provided in Fig. 16 and Fig. 17, respectively. The analytical damage maps are from select output frames that illustrate the predicted damage evolution. In both the G_{c} and G_{R} analyses, damage initiates at all four locations along the stiffener flange edges where the post-buckled shape causes the skin panel to pull away from the stiffener. Similar to the pristine analysis results, the damage state in the G_{c} analysis is split between skin/stiffener interface and the first interface of the skin panel, with the majority of the damage being on the first interface of the skin panel. The damage front grows along the stiffener flange edge and further underneath the stiffener until the unstable propagation occurs (Fig. 16c). The G_{R} analysis prediction again comprises predominantly matrix cracks and delaminations on the first interface of the skin panel. The damage front grows to a smaller size in the G_{R} analysis results (Fig. 17b) before propagating unstably (Fig. 17c).

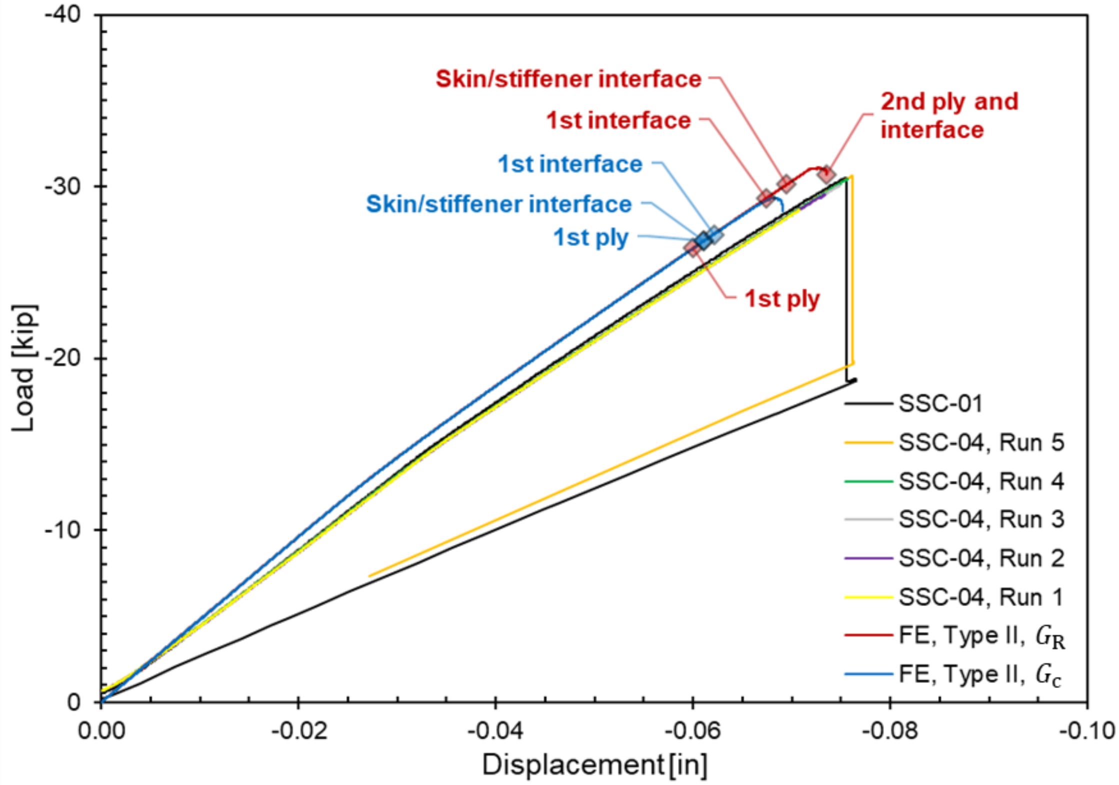

Fig. 14 Test and analysis load/displacement histories for Teflon specimens with the Type II buckling shape.

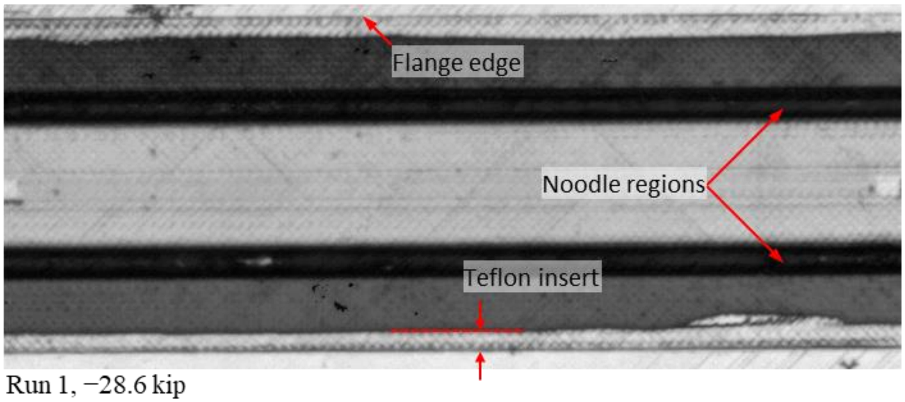

a) Run 1, −28.6 kip

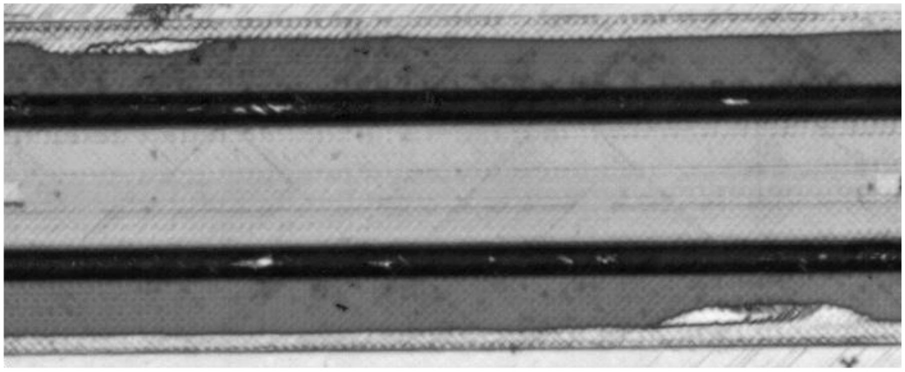

b) Run 2, −29.5 kip

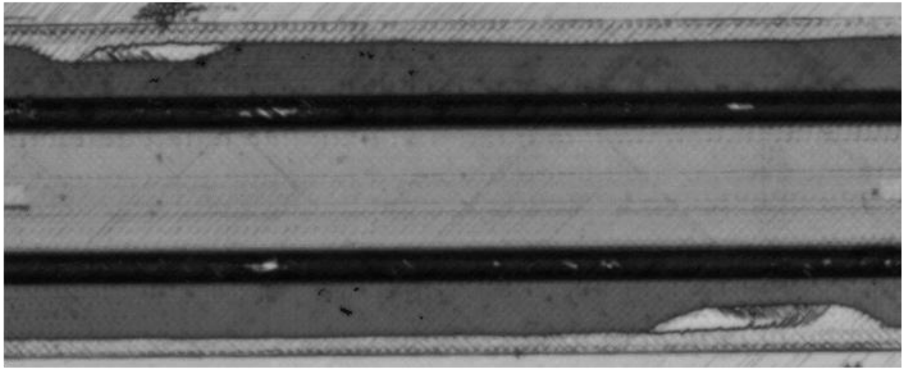

c) Run 3, −30.0 kip

Fig. 15 UT scans for Teflon specimen SSC-04, with the Type II buckling shape.

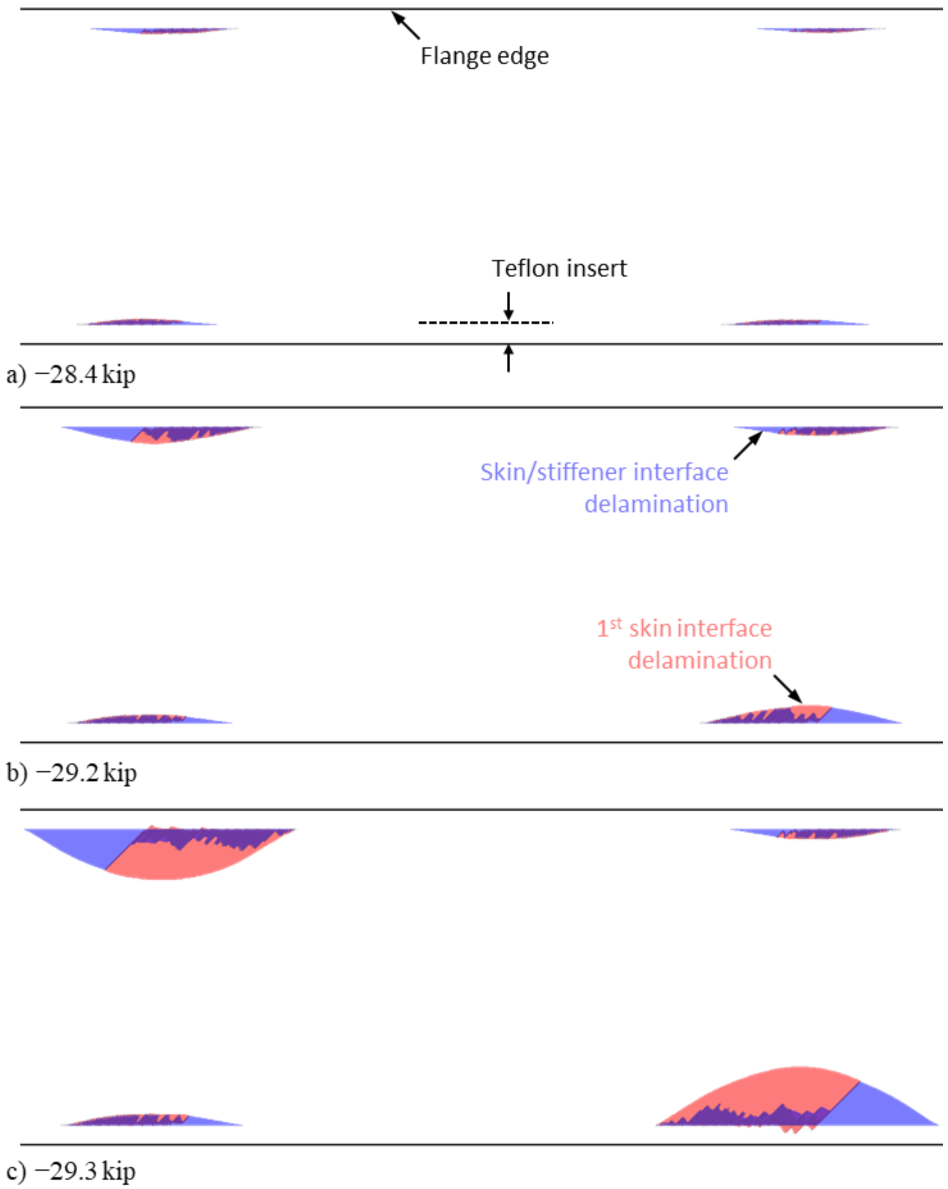

Fig. 16 **Damage maps for Teflon specimen analyses with Type II buckling and G_c tape/fabric interface fracture properties.**

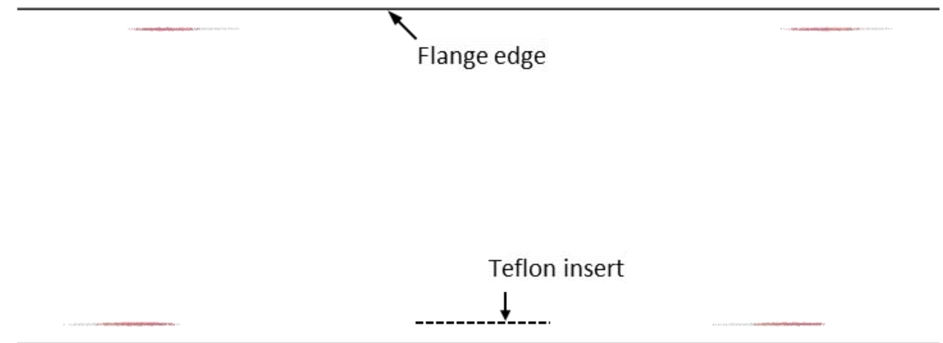

a) −30.5 kip

b) −30.9 kip

c) −31.1 kip

Fig. 17 Damage maps for Teflon specimen analyses with Type II buckling and G_R tape/fabric interface fracture properties.

Quantitative comparisons of the damage lengths as measured along the stiffener flange edges are provided in Fig. 18 for the Teflon specimen experimental results and the corresponding G_c and G_R analyses. The load range in which the initiation and pre-peak stable growth of damage was observed in the tests is small with respect to the peak test loads for both buckling shapes. For the Type I buckling shape, damage was first observed in the tests at 92% of the peak load, Fig. 18a. For the Type II buckling shape, damage was first observed at 94% of the peak load, Fig. 18b. The initial lengths of the damage in the test specimens ranged from 1 to 2 inches. There are too few measurements for the Type I buckling shape to identify a growth rate, but a steady rate of change in damage length versus peak load can be identified for specimen SSC-04, Fig. 18b. The damage grew steadily from initiation to ultimate failure in all of the Teflon analysis results. The analysis peak loads from the G_R analyses match the experimental results slightly better than the G_c analyses, though both the damage lengths and morphology in the G_c analyses better match the test results.

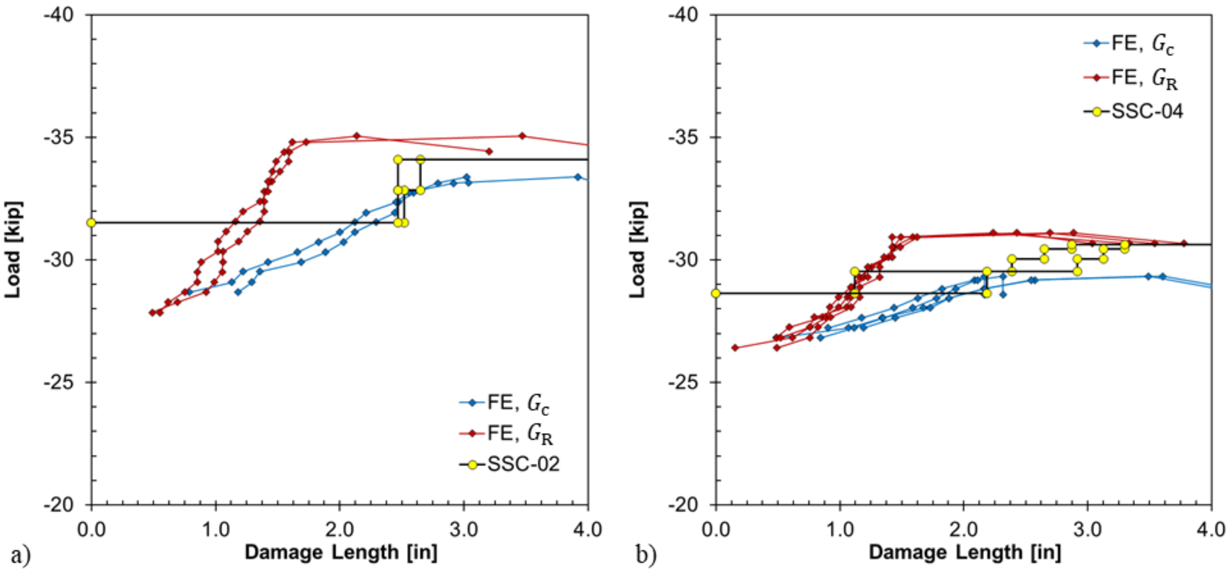

Fig. 18 Load versus damage length for Teflon tests and analyses for the (a) Type I and (b) Type II buckling shapes. Damage lengths are measured along the length of the stiffener flange edges.

C. Impact damage

The initial impact damage of specimen SSC-03 was characterized by UT inspection and X-ray CT. The initial impact damage comprised delaminations on the skin/stiffener interface and the first interface within the skin panel, and matrix cracks in the first 45° ply of the skin panel. The UT amplitude data taken from the skin-side of the specimen in Fig. 19a was used to define the interlaminar damage. The locations, lengths, and through-thickness orientation of the initial matrix cracks were determined via X-ray CT. The damage in each of these regions was mapped to an element set for which the damage variables were initialized to represent the damage, Fig. 19b.

Specimen SSC-03 was loaded five times, failing on the fifth loading at a peak load of −38.4 kip. The load/displacement responses of the five test loadings and the two corresponding analyses are shown in Fig. 20. The UT amplitude scan data from the first four loadings in Fig. 21 reveal steady and substantial growth from the initial impact site. The first observed damage growth from the initial impact state occurred at 94% of the peak load, Fig. 20a. The damage then grew to a length comparable to that observed in specimen SSC-04 (Fig. 21b). This length corresponds to the portion of the specimen in which the skin panel is buckling away from the stiffener in the Type II shape. After the fourth loading, a small amount of skin/stiffener interface damage outside of the initial image region is visible in the UT amplitude data in Fig. 21d. From this location of damage initiation outside the initial impact area, the damage then propagated unstably, failing the specimen.

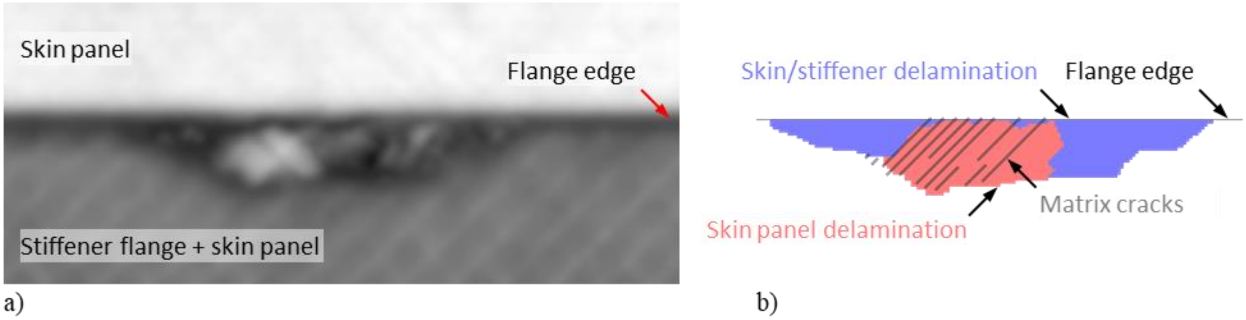

Fig. 19 Initial impact damage specimen SSC-03 (a) as scanned by UT and (b) as mapped into the FE mesh.

The analyses with both tape/fabric interface properties underpredict the experimental peak load, with predicted peak loads of −32.2 and −33.8 kip for the G_{c} and G_{R} property sets, respectively. Both predicted peak loads are below the experimental load at which damage growth from the initial impact state was first observed (−36.1 kip). In order to compare the experimental and analytical damage evolution processes, damage maps for the G_{c} and G_{R} analyses are presented in Fig. 22 and Fig. 23 at analysis output frames at which the analyses predict significant changes in the damage morphology and/or size. In the G_{c} analysis, the initial impact damage first grows along the stiffener flange edge on the skin/stiffener interface and inward toward the stiffener center by migrating down to the first interface of the skin panel via a series of matrix cracks, Fig. 22a and Fig. 22b. The G_{c} analysis damage state then develops in Fig. 22c to resemble the Type II Teflon prediction in Fig. 16b, and continues to grow in a similar fashion until the predicted peak load. Damage initiation is predicted outside of the initial impact region, though it is the impact damage that is predicted to eventually propagate unstably. Similar to the pristine and Teflon predictions, the damage morphology of the impact analysis with the tougher G_{R} properties is dominated by delamination on the first interface of the skin panel, connected to the stiffener flange termination by a series of matrix cracks, as shown in Fig. 23.

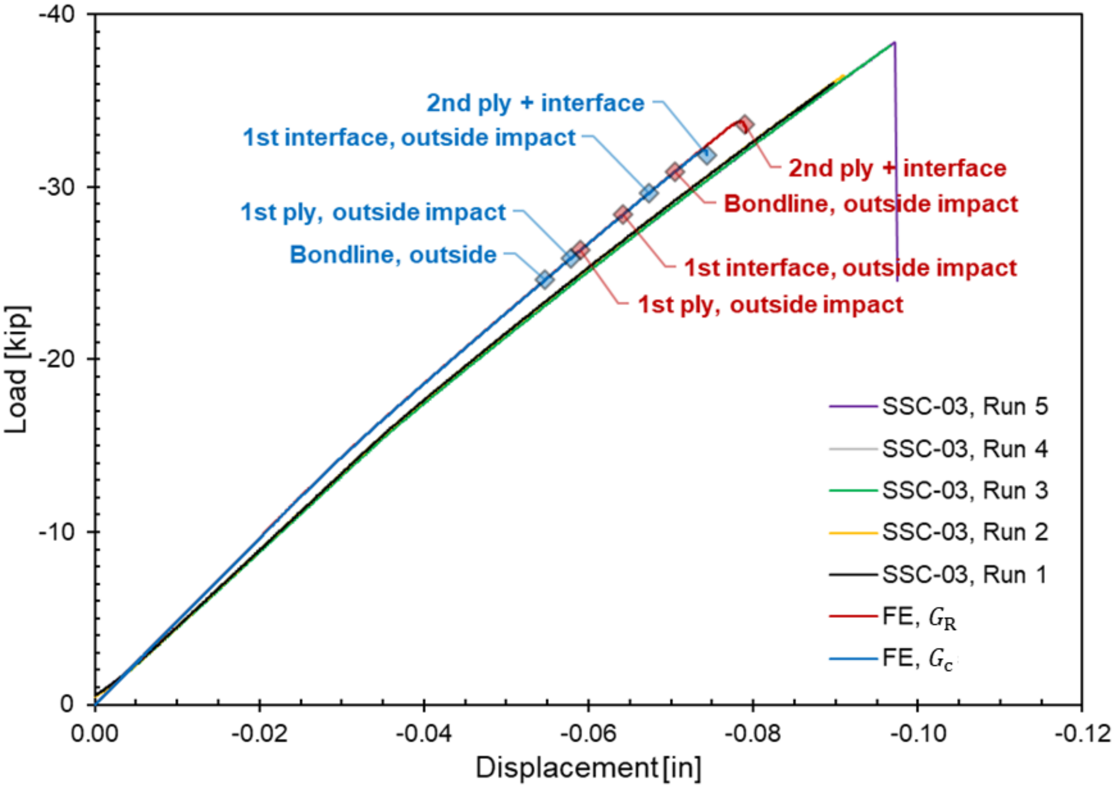

Fig. 20 Test and analysis load/displacement histories for impact specimens.

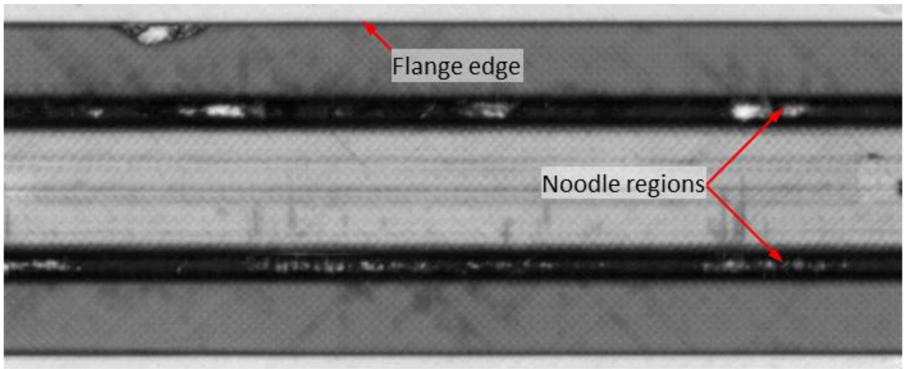

a) Run 1, −36.1 kip

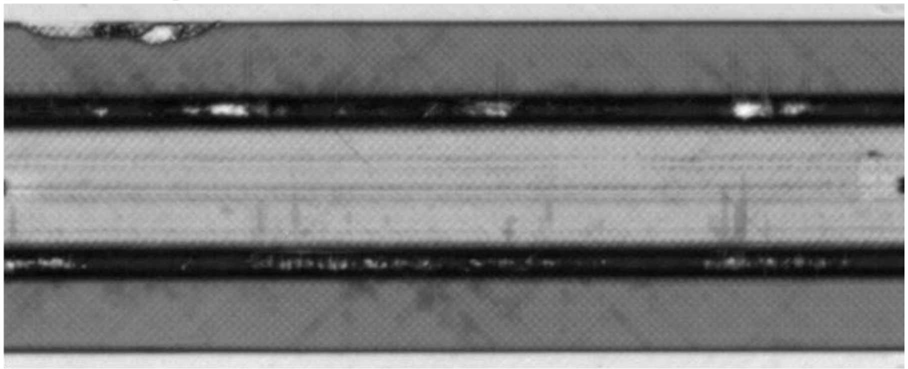

b) Run 2, −36.5 kip

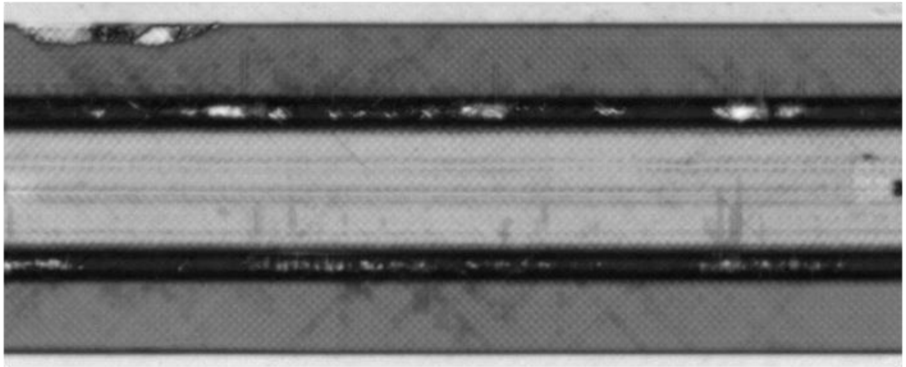

c) Run 3, −38.2 kip

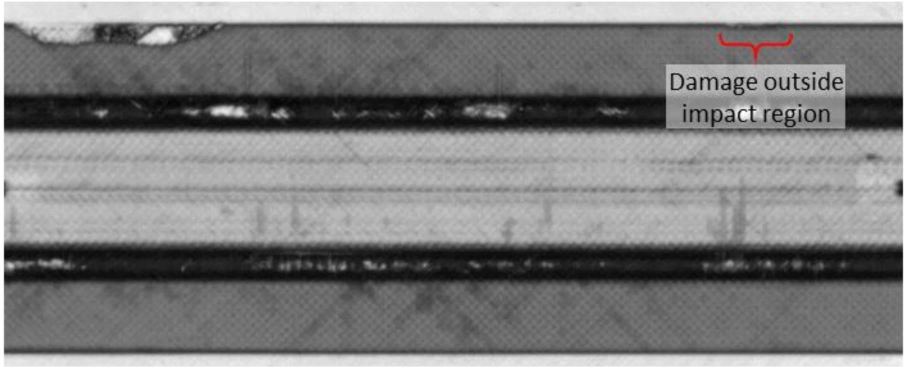

d) Run 4, −38.2 kip

Fig. 21 UT scans for impact specimen SSC-03.

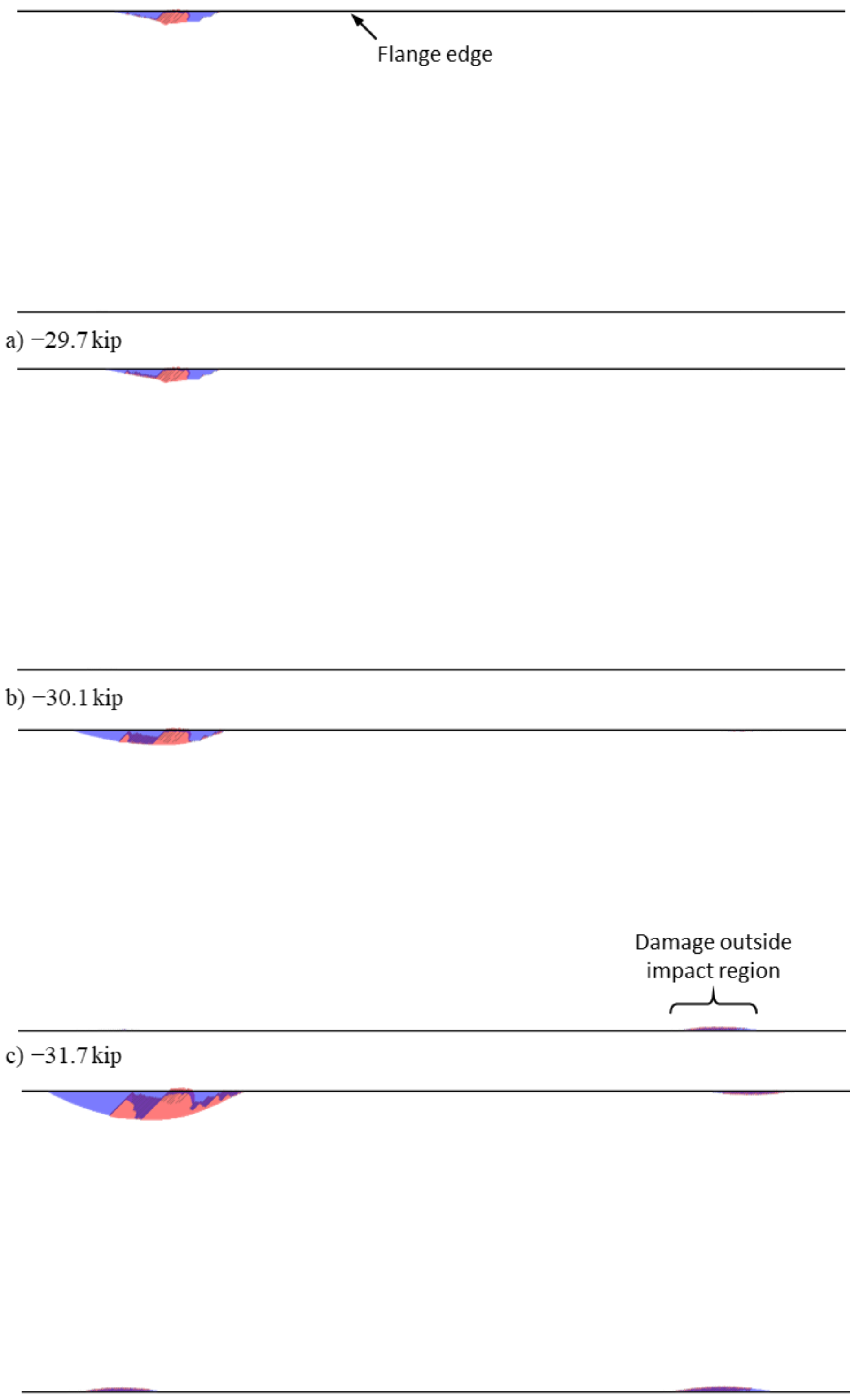

a) −29.7 kip

b) −30.1 kip

c) −31.7 kip

d) −32.1 kip

Fig. 22 Damage maps for impact specimen analyses with the G_c tape/fabric interface fracture properties.

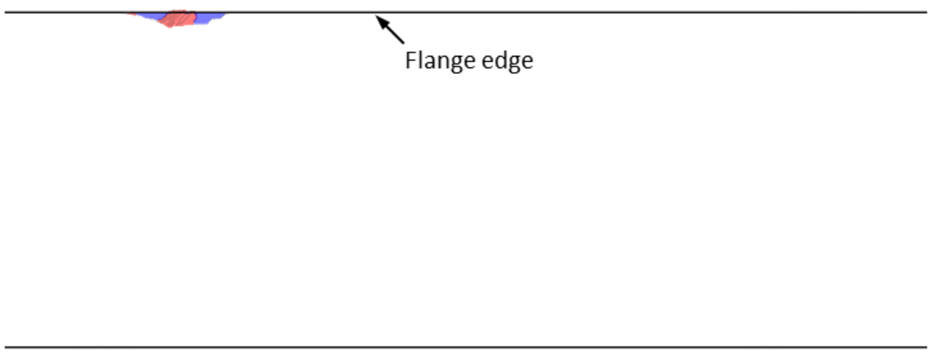

a) −30.9 kip

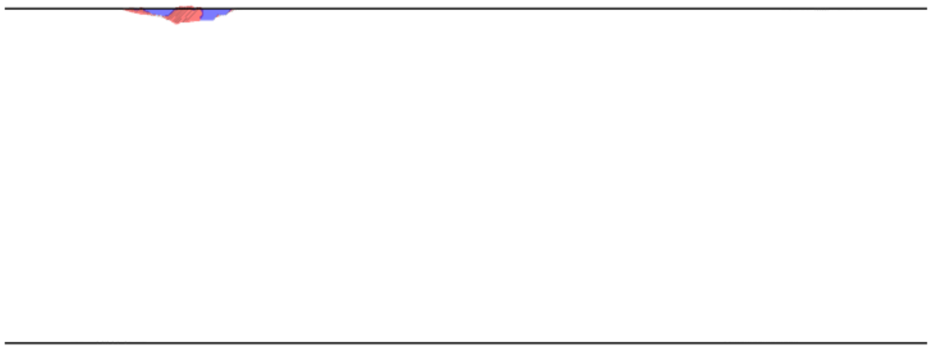

b) −32.2 kip

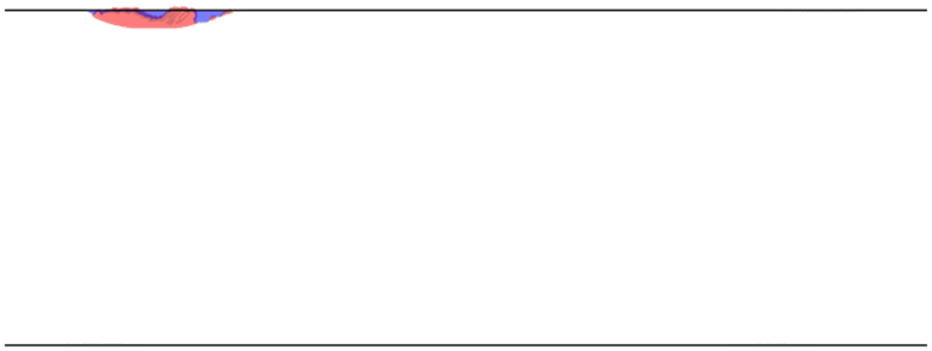

c) −33.0 kip

d) −33.7 kip

Fig. 23 Damage maps for impacted specimen analyses with G_R tape/fabric interface fracture properties.

Test and analysis damage length comparisons are provided in Fig. 24. Analytical load versus damage length curves for the impacted and initially pristine quadrants of the models are plotted. Again, both analyses under-predicted the test peak loads, though the G_c analysis results agree well both in terms of damage growth rate from initiation to unstable failure and in terms of overall damage morphology throughout the damage evolution process.

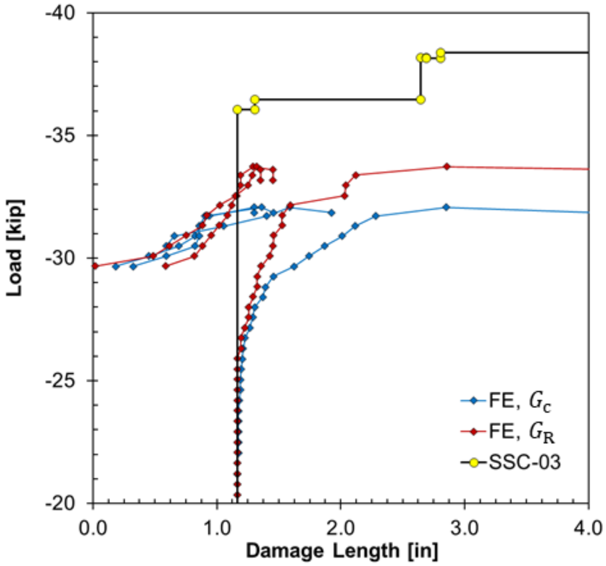

Fig. 24 Load versus damage length for an impacted specimen (SSC-03) and analyses.

V. Closing Remarks

The single stringer compression test data reveals that the initiation and evolution of damage occurs in only the top five percent of the specimen strength for the specimen design and materials used in this study. As such, the characterization of multiple intermediate damage states requires significant technical precision in terms of experimental setup, real-time monitoring, and nondestructive inspection. The pristine single stringer specimen tests did not yield any pre-peak damage morphology data, limiting the test/analysis correlation to load/displacement history comparisons. Comparing experimental and analytical load/displacement histories is insufficient for the validation of progression damage analyses. Fortunately, the Teflon-insert and impacted specimen tests yielded richer pre-peak damage data. The best overall test/analysis correlation, considering both damage morphology and load/displacement history, was achieved for the Teflon-insert cases. The test/analysis correlation for the Teflon-insert specimens benefitted from each specimen yielding damage growth data from each post-buckled half-wave that buckled away from the skin, whereas only one location of the impact specimen yielded damage growth data.

The test and analysis damage morphologies of the single stringer specimens in this project are extremely self-consistent, regardless of initial damage configuration and post-buckled shape. That is, the same multi-interface damage state develops within post-buckled half-waves in which the skin panel buckles away from the stiffener in each of the tests and the G_c analyses. The damage morphology within the G_R analyses differs from the tests, but has the same general configuration for the Type I and Type II buckling shapes and each of the three initial damage configurations. Furthermore, the damage morphologies for the single stringer specimens are the same as those experimentally observed and predicted for the seven-point bend specimens [4]. The consistency of the damage morphologies between the seven-point bend and single stringer compression specimens suggests that the seven-point bend specimen accurately represents the initiation and propagation of damage in post-buckled structures, while allowing for stable damage growth and, therefore, more easily provides more data for progressive damage analysis tool validation.

Acknowledgments

The authors thank William Johnston, Helen Herring, Joseph Zalameda, Michael Horne and all those who contributed to the testing and characterization of the single stringer compression specimens in support of the NASA ACP.

References

[1] S. Wanthal, J. Schaefer, B. Justusson, I. Hyder, S. Engelstad and C. Rose, "Verification and Validation Process for Progressive Damage and Failure Analysis Methods in the NASA Advanced Composites Consortium," in 32nd American Society for Composites Technical Conference, West Lafayette, IN, 2017.

[2] J. Action, W. Jackson, J. Zalameda and U. Palliyaguru, "Testing of a Multi-Stringer Post-Buckled Panel," in AIAA SciTech Forum, Orlando, FL, 2020.

[3] A. S. Selvarathinam, N. V. De Carvalho, B. R. Seshadri, V. Johnson, W. M. Johnston, W. C. Jackson, C. A. Rose and T. K. O'Brien, "Validation of Floating Node Method Using Three-Point Bend Doubler Under Quasi-Static Loading," in AIAA SciTech Forum, San Diego, CA, 2019.

[4] F. A. Leone, K. Song, W. Johnston, C. A. Rose, W. C. Jackson and C. G. Davila, "Test/Analysis Correlation of Damage States in Post-buckled Stiffened Validation Building Block Specimens," in 34th American Society for Composites Technical Conference, Atlanta, GA, 2019.

[5] J. N. Zalameda, W. P. Winfree and M. R. Horne, "Detection of Damage During Quasi-Static Loading of a Single Stringer Panel Using Passive Thermography and Acoustic Emission," in SEM Annual Conference and Exposition on Experimental and Applied Mechanics, Greenville, SC, 2018.

[6] F. A. Leone, C. G. Dávila, G. E. Mabson, M. Ramnath and I. Hyder, "Fracture-Based Mesh Size Requirements for Matrix Cracks in Continuum Damage Mechanics Models," in AIAA SciTech Forum, Grapevine, TX, 2017.

[7] F. A. Leone, A. C. Bergan and C. G. Dávila, *CompDam - Deformation Gradient Decomposition (DGD), v2.5.0,* 2019.

[8] B. Justusson, I. Hyder, S. Boyd and F. Leone, "Quantification of Error Associated with Using Misaligned Meshes in Continuum Damage Mechanics Material Models for Matrix Crack Growth Predictions in Composites," in 33rd American Society for Composites Technical Conference, Seattle, WA, 2018.

[9] I. Hyder, F. Leone, B. Justusson, J. Schaefer, A. C. Bergan and S. Wanthal, "Implementation of a Matrix Crack Spacing Parameter in a Continuum Damage Mechanics Finite Element Model," in 33rd American Society for Composites Technical Conference, Seattle, WA, 2018.

[10] G. B. Murri, "Evaluation of Delamination Onset and Growth Characterization Methods under Mode I Fatigue Loading," NASA/TM–2013-217966, Hampton, VA, February 2013.

[11] T. K. O'Brien, W. M. Johnston and G. J. Toland, "Mode II Interlaminar Fracture Toughness and Fatigue Characterization of a Graphite Epoxy Composite Material," NASA/TM–2010-216838, Hampton, VA, August 2010.

[12] J. G. Ratcliffe and W. M. Johnston, "Influence of Mixed Mode I-Mode II Loading on Fatigue Delamination Growth Characteristics of a Graphite Epoxy Tape Laminate," in 29th American Society for Composites Technical Conference, San Diego, CA, 2014.

[13] S. T. Pinho, C. G. Dávila, P. P. Camanho, L. Iannucci and P. Robinson, "Failure Models and Criteria for FRP Under In-Plane or Three-Dimensional Stress States Including Shear Nonlinearity," NASA/TM-2005-213530, Hampton, VA, February 2005.

[14] A. C. Bergan, "Computational Performance of Progressive Damage Analysis of Composite Laminates using Abaqus/Explicit with 16 to 512 CPU Cores," NASA/TM-2019-220251, Hampton, VA, February 2019.